Biointerface Research in Applied Chemistry
Open-Access Journal (ISSN: 2069-5837)

Article
Volume 13, Issue 1, 2023, 6
https://doi.org/10.33263/BRIAC131.006

Cytotoxicity, Antioxidant Activity, Molecular Docking, and Dynamics Simulation Analysis Against SARS-CoV-2 M and N Protein Models of Phytoconstituents of *Micromelum Minutum*

Fatema-Tuz-Zohora [1,2,*], Rumana Mahtarin [3], Md Ackas Ali [3], Mohammad Johirul Islam [4], Md. Hossain Sohrab [5], Choudhury Mahmood Hasan [1], Monira Ahsan [1]

1 Department of Pharmaceutical Chemistry, University of Dhaka, Dhaka-1000, Bangladesh; fatema.zohora41@gmail.com (F.T.Z.), cmhasan@gmail.com (C.M.H.), ahsanm80@yahoo.com (M.A.);
2 Primeasia University, Department of Pharmacy, Star Tower, 12 Kemal Ataturk Avenue, Dhaka 1213, Bangladesh; fatema.zohora@primeasia.edu.bd (F.T.Z.);
3 Division of Infectious Diseases and Division of Computer-Aided Drug Design, The Red-Green Research Centre, BICCB, Tejgaon, Dhaka, Bangladesh; rumana.trisha@gmail.com (R.M.), akashali16dec@gmail.com (M.A.A.);
4 Department of Pharmacy, State University of Bangladesh, Sobhan Tower, 138 Mirpur Rd, Dhaka 1205, Bangladesh; johir.647.ji@gmail.com (M.J.I.);
5 Bangladesh Council of Scientific and Industrial Research (BCSIR), Dr.Qudrat-E-Khuda Road, Dhaka 1205, Bangladesh, mhsohrab@bcsir.gov.bd (M.H.S.);
* Correspondence: fatema.zohora41@gmail.com (F.T.Z);

Scopus Author ID 57207665564
Received: 5.10.2021; Accepted: 31.10.2021; Published: 7.01.2022

Abstract: Phytochemical investigations of the methanolic extract of the whole plant of *Micromelum minutum* provided two coumarins, namely micromelin and murrangatin, and one sterol stigmast-4-en-3-one, the latter being reported for the first time from *M. minutum*. To evaluate bioactivities, different fractions of the crude methanol extracts of the plant obtained by partitioning were screened for antioxidant and cytotoxic activity by DPPH radical scavenging method and the brine shrimp lethality bioassay, respectively. Among the different fractions of *M. minutum* tested, pet ether and chloroform soluble fractions showed prominent antioxidant activities with IC_{50} values of 49.46 and 67.53 µg/mL compared to the standard butylated hydroxytoluene (IC_{50} 31.02 µg/ml). The pet ether and chloroform fractions of *M. minutum* showed good brine shrimp larvicidal activity with LC_{50} values of 1.15 and 1.50 µg/ml, respectively, compared to vincristine sulfate (LC_{50} 0.27 µg/ml). The results obtained from molecular docking, Stigmast-4-en-3-one exerts the highest negative binding affinity (-9.1 kcal/mol) for interaction with SARS-CoV-2 M protein and develops a strong network with eleven hydrophobic bonds established by ADMET profile studies and YASARA Dynamics program.

Keywords: *Micromelum minutum*; stigmast-4-en-3-one; ADMET profiling; MD simulation; SARS-CoV-2 M protein.

1. Introduction

SARS-Cov-2 is the causative agent responsible for the 2019-2021 viral pneumonia outbreak COVID-19 [1]. Currently, there are no targeted therapeutic agents for this disease, and effective treatment options remain very limited [2]. The fast-spreading nature of severe acute respiratory syndrome coronavirus 2 has created a massive calamity in recent times [3].

During viral replication and assembly, the structural proteins play a crucial role in associating viral particles [4]. One of the central functional constituents is membrane protein (M) which significantly maintains virion size and shape. The protein accumulates other structural proteins inclosing spike (S), envelope (E), and nucleocapsid (N) [5-8], and takes part in the budding process [9]. Virus-like particle (VLP) of coronaviruses developed by the cooperative interaction of M and E or M and N proteins. The mutual expression of M, N, and E is compulsory for efficient VLP production and its trafficking and release [10]. Besides, another multifunctional protein has been recognized as SARS-CoV-2 nucleocapsid protein (N). Usually, the protein potentially binds to the viral RNA genome and folds it into the RNP complex [11]. Hence, membrane protein (M) and nucleocapsid (N) protein of SARS-CoV-2 are considered potential drug targets [12]. On the other hand, the *Micromelum* species are recognized to contain 8- and 6-prenylated coumarins [13]. The present work has exploited the isolation and structural determination of some of the secondary metabolites present in the plant of *Micromelum minutum*. In this study, we have also investigated the probable effectiveness of our experimental compounds from *Micromelum minutum* species through *in silico* approaches such as molecular docking, ADMET profiling followed by molecular dynamics (MD) simulation.

2. Materials and Methods

^{1}H NMR and ^{13}C NMR spectra were recorded on Bruker AV-400 spectrometers at a frequency of 400 MHz and 100 MHz, respectively. Chemical shifts are expressed in ppm, and *J* values are given in Hz. Analytical TLC plates with silica gel 60 F_{254} TLC (Merck, Germany) were used to determine TLC profiles. The spots on TLC plates were visualized using a UV lamp (254 and 366 nm). Column chromatography was performed at silica gel (270 mesh). All chemicals, solvents, and reagents were used to the analytical grade level.

The whole plant of *M. minutum* was collected from various regions of Khagrachari District, Chittagong Hill Tracts of Bangladesh in January 2015. Both of the plants were identified by an expert at the Bangladesh National Herbarium, and a voucher specimen was deposited for this collection. The accession number of *M. minutum* is DACB-41589.

750 gm of powdered whole plant material of *M. minutum* were taken in clean, amber-colored bottles and soaked in distilled methanol for 40 days, occasionally shaken and stirred. Then the mixture was filtered through a fresh cotton plug and reduced the volume of the filtrate using a Buchi rotary evaporator. The ethyl acetate (EtOAc) soluble fraction (4.5 g) and chloroform ($CHCl_3$) soluble fraction (6 g) from the crude methanolic extract (14 g) was sequentially separated out by continuous stirring with (100:0, v/v) each solvent. The entire ethyl acetate soluble fraction (4.5 g) was fractionated by silica column chromatography (CC) [n-hexane- CH_2Cl_2 gradient (100:0–0:100, v/v) to CH_2Cl_2-EtOAc (99:1–0:100, v/v) to EtOAcMeOH (99:1–20:80, v/v)] to afford 75 fractions or test tubes each with 20 ml solvent system. Evaporation of solvents of CC fractions 22 to 31 (CH_2Cl_2 in EtOAc, 75:25–0:100, v/v) furnished impure colorless crystalline mass. Repeated washing of these crystalline masses with n-hexane-$CHCl_3$ (60:40, v/v) and then recrystallized with n-hexane and ethyl acetate (50:50, v/v) yielded pure crystals named as compound **1**(30 mg, R_f= 0.41). After evaporating of the solvents of silica column fractions of 53 to 69 (EtOAc in MeOH, 75:25–63:69, v/v) give colorless crystal of compound **2** (10 mg, R_f = 0.31). Fraction 1 to 15 (n-hexane in CH_2Cl_2, 100:00–97:3.0, v/v) were mixed together subjected to TLC run with toluene/EtOAc (99:1) for two times to yield compound **3** (11.9 mg, R_f= 0.50).

Solvent-solvent fractionation of the crude methanolic extract was accompanied by using the modified Kupchan method [14]. Methanolic crude (5g) extract was triturated with ninety percent methanol. The acquired solution was at that time fractionated in sequence using solvents of growing polarization such as pet-ether (PE), carbon tetrachloride (CTC), and chloroform (CF).

Antioxidant activities of the plant extract on the stable radical 1,1- diphenyl- 2-picrylhydrazyl (DPPH) were assessed by mixing 2.0 ml of methanol solution of the extract at various concentrations with 2.0 ml of a DPPH methanol solution (20 µg/ml). The antioxidant potential was evaluated from the fading of purple-colored methanol solution of DPPH radical by the plant extract compared with butylated hydroxytoluene (BHT) by UV spectrophotometer [15].

The brine shrimp lethality bioassay principle was established on the killing ability of test samples on a biological organism brine shrimp (*Artemia salina* Leach) nauplii. In this assay, the different concentrated samples were added to a series of test tubes containing a fixed number of nauplii. The number of survived nauplii was counted up after 24 hours. From each sample concentration and control (containing no sample), the percent (%) of the lethality of the nauplii was calculated [16, 17].

The predicted 3D structure of SARS-CoV-2 M protein was constructed from the trRosetta server to conduct molecular docking simulation. The structure was directly energy minimized with restrained (inter-residue distance and orientation distributions) Rosetta by a deep residual neural network [18-20]. An all-atom model of SARS-CoV-2 N protein was collected from the I-TASSER server [21]. The structure with the lowest energy was assembled via REMO by optimizing the hydrogen-bonding network. The initial geometries of the selected compounds from *M. minutum* species were collected from the PubChem database. Quantum mechanics (QM) calculations were conducted to optimize the compounds. Gaussian 09 program package was applied for all quantum calculations [22]. The semi-empirical PM6 method [23] was used for optimization. In harmonic approximation, the vibrational frequencies were calculated, ensuring the absence of imaginary frequencies.

The molecular docking was performed for full-length M (trRosetta model) and N (I-TASSER model) structural proteins with stigmast-4-en-3-one sterol, micromelin, and murrangatin coumarins. The binding affinities and the interactions of the selected compounds were predicted via the Auto Dock Vina protocol [24-26]. During docking, the grid box for M protein was set around the residues Phe103, Arg107, Met109, Trp110, Arg131, and Glu135, which were commonly interacting with S and N proteins [10], within the vina search space, including center X= 41.38 Å, Y= 76.16 Å, and Z= 40.71 Å and dimensions were X: 34.16 Å, Y: 61.36 Å, and Z: 35.24 Å. For N protein, the grid box value remained around center X= -40.22 Å, Y= 7.13 Å, and Z= -36.46 Å and where the dimensions were X: 41.88 Å, Y: 48.07 Å, and Z: 47.53 Å covering binding site residues in N-CTD (dimerization and RNA binding domain) [5]. The non-covalent interactions in the docked complex were visualized by BIOVIA Discovery Studio version 4.5 [27, 28].

The major ADMET properties for the preferred compounds were developed from their graph-based signatures through the pkCSM server. ADMET profiles outline the absorption, distribution, metabolism, excretion, and toxicity properties. Understanding the pharmacokinetics, toxicity, and potency of drugs is essential to mitigate the risk of attrition for effective drug development [29]. The SMILE file formats of the compounds were retrieved from the PubChem database (www.pubchem.ncbi.nlm.nih.gov) for the analysis [30]. pkCSM

server predicts various properties, e.g., solubility, human intestinal absorption (HIA), the human Ether-a-go-go-Related Gene (hERG), Caco-2 permeability, central nervous system (CNS) permeability, cytochrome P450 [31] enzyme inhibition level, and P glycoprotein inhibitor (PGI), AMES toxicity, max. tolerated dose (human), and hepatotoxicity of the compounds.

Molecular dynamics simulation of apo M, N protein and their complex with stigmast4-en-3-one compound were performed in the YASARA Dynamics program [32]. The AMBER14 force field was applied for all calculations [33]. The simulation environment was equilibrated with 0.9% NaCl and water solvent at 298 K temperature. The time step was 1.25 fs during 50 ns MD simulation, and 500 snapshots were obtained at 100 ps time interval. Berendsen's thermostat process was applied to regulate the simulation temperature [34]. The particle mesh Ewald algorithm was employed for long-range electrostatic interactions. The short-range van der Waals and Coulomb interactions were determined at an 8.0 Å cut-off radius. A periodic boundary condition was adopted during the simulation of membrane-embedded protein. YASARA exhibited the recommended membrane embedding by scanning for hydrophobic residues and assembled a membrane of 69.2 Å×7.3 Å with the lipid composition of phosphatidyl-ethanolamine. An equilibration simulation continued for 250 ps. The membrane was stabilized to adjust the protein and preserve the exact density throughout the equilibration phase. Later, root mean square deviation (RMSD), root mean square fluctuation (RMSF) trajectories were analyzed.

3. Results and Discussion

Three compounds (**1**-**3**) from the ethyl acetate soluble fractions of crude methanolic extract of *Micromelum minutum* were isolated, and the structures of the compounds were elucidated by NMR spectroscopy (^{1}H, ^{13}C NMR, ^{1}H-^{1}H COSY, HSQC, HMBC).

3.1. Characterization of isolated compounds.

Compound **1**, was obtained as colorless crystals. It appeared as a blue spot on a TLC plate under UV light at 254 nm and a blue fluorescent spot at 366 nm. The ^{1}H NMR spectrum (400 MHz, $CDCl_3$; Table 1 and Figure S9) showed two doublets at δ 6.34 (*J* = 9.5 Hz) and 7.67 (*J* = 9.5 Hz), corresponding to H-3 and H-4, indicating two olefinic protons of an α-pyrone ring of a coumarin. The presence of two aromatic singlets at δ 7.39 and 6.90 were attributable to H-5 and H-8, indicating a 6,7-disubstituted coumarin nucleus. The spectrum further showed a methoxy group at δ 3.93 and a deshielded methyl at δ 1.69. The downfield shift of the latter was consistent with its close proximity to an epoxide ring and a carbonyl group. In the ^{1}H NMR spectrum, the sharp singlets at δ 4.06 and 5.58 were assigned to H-4' and H-5' protons, respectively. The ^{1}H NMR data were consistent with those reported for micromelin [35], and thus compound **1** was identified as micromelin.

Compound **2**, isolated as colorless crystals, presented a deep blue fluorescent spot at 366 nm UV light on a TLC plate and gave ash color when sprayed with vanillin in sulphuric acid reagent followed by heating for 2 minutes. The ^{1}H NMR spectrum (400 MHz, CD_3OD; Figure S10) displayed two doublets at δ 6.27 (*J* = 9.2 Hz) and 7.91 (*J* = 9.2 Hz), indicating two olefinic protons of an α-pyrone ring could be allocated to H-3 and H-4 protons of the coumarin nucleus respectively. The aromatic proton doublets at δ 7.58 (*J* = 8.4 Hz) and 7.10 (*J* = 8.4 Hz), assignable to H-5 and H-6 respectively, indicated a 7,8 disubstituted coumarin. The spectrum

also showed a methoxy group at δ 3.98 (3H s). Another two doublets at δ 5.40 (*J* = 8.8 Hz) and 4.74 (*J* = 8.8 Hz), a venylic methyl at δ 1.92, and an exomethylene group at δ 5.11 and 5.10 suggested the presence of a 1, 2-dihydroxy-3methylbut-3-enyl chain. Thus compound 2, was identified as 7-methoxy-8-(1, 2-dihydroxy-3-methylbut-3-enyl) coumarin or murrangatin. The ^{13}C spectrum displayed all the 15 carbons (Table 1; Figure S10.1), including one carbonyl carbon at δ 161.8, two carbinol carbons at δ 66.4 & 76.5, and one methylene carbon at δ 117.1. The clear assignments of all the carbons and protons followed from COSY (Figure S10.2), HMBC (Figure S10.3), and HSQC (Figure S10.4) experiments. In the HMBC experiment, H-1' proton showed ^{2}J correlation to C-8 and ^{3}J correlations to H-7 and H-9, thus confirming the position of the 5-carbon moiety, 1, 2dihydroxy-3-methylbut-3-enyl chain at C-8. The ^{1}H and ^{13}C data of compound **2** were consistent with those reported for murrangatin, a previously known compound from *M. minutum* [36, 37, 38].

Compound **3** was isolated as a colorless crystal and produced purple color when sprayed with vanillin in sulphuric acid reagent, followed by heating for 2 minutes (Figure S1).

The ^{1}H NMR spectrum of compound **3** (400 MHz, $CDCl_3$; Table 1; Figure S11 and Figure S11.1) displayed signals for six methyl groups at δ 0.73 s, 0.88 d (*J* = 7.2 Hz), 0.86 d (*J* = 7.2 Hz), 0.87 t (*J* = 7.2 Hz), 0.95 d (*J* = 6.4 Hz) and 1.20 attributable to H-18, H-27, H-26, H-29, H-21 and H-19 respectively. An olefinic proton appeared as a sharp singlet at δ 5.74, assignable to H-4. The ^{1}H NMR spectrums were found similar to those reported for stigmast-4-en-3-one [39]. Thus compound **3**, was identified as stigmast-4-en-3-one. Stigmast-4-en-3-one is isolated for the first time from *M. minutum*.

Table 1. NMR spectral data for compound **1**, **2** and **3**.

Position	δ_H[a] (2)	δ_C[b] (2)	HMBC (2)	δ_H[a] (1)	δ_H[a] (3)
2		161.8			
3	6.27 d (*J* = 9.2 Hz)	111.8	161.8 (C-2), 113.1 (C-10)	6.34 d (*J* = 9.5 Hz)	
4	7.91 d (*J* = 9.2 Hz)	144.9	161.8 (C-2), 111.8 (C-3), 117.1 (C-8), 128.6 (C-5), 153.4 (C-9)	7.67 d (*J* = 9.5 Hz)	5.74 s
5	7.58 d (*J* = 8.4Hz)	128.6	111.8 (C-3), 144.9 (C-4), 108.2 (C-6), 117.1 (C-8), 153.4 (C-9), 161.5 (C-7)	7.39 s	
6	7.10 d (*J* = 8.4Hz)	108.2	161.5 (C-7), 117.1 (C-8), 153.4 (C-9), 113.1 (C-10), 76.5 (C-2')		
7		161.5			
8		117.1		6.90 s	
9		153.4			
10		113.1			
1'	5.40 d (*J* = 8.8 Hz)	66.4	161.5 (C-7), 117.1 (C-8), 153.4 (C-9), 76.5 (C-2'), 145.9 (C-3')		
2'	4.74 d (*J* = 8.8 Hz)	76.5	117.1 (C-8), 66.4 (C-1'), 145.9 (C-3'), 117.1 (C-4'), 16.2 (Me-3')		
3'		145.9			
4'	5.11 br s 5.00 br s	117.1	16.2 (Me-3'), 76.5 (C-2')	4.06 s	

Position	δ_H[a] (2)	δ_C[b] (2)	HMBC (2)	δ_H[a] (1)	δ_H[a] (3)
5’				5.58 s	
Me-3’	1.92 3H s	16.2	76.5 (C-2’), 145.9 (C-3’), 117.1 (C-4’)	1.69 s	
OMe-7	3.98 3H s	55.4	108.2 (C-6), 161.5 (C-7)	3.97 s	
18					0.73 s
19					1.20 s
21					0.95 d (*J* = 6.4 Hz)
26					0.86 d (*J* = 7.2 Hz)
27					0.88 d (*J* = 7.2 Hz)
29					0.87 t (*J* = 7.2 Hz)

[a] = measured in 400 MHz, [b]= measured in 100 MHz

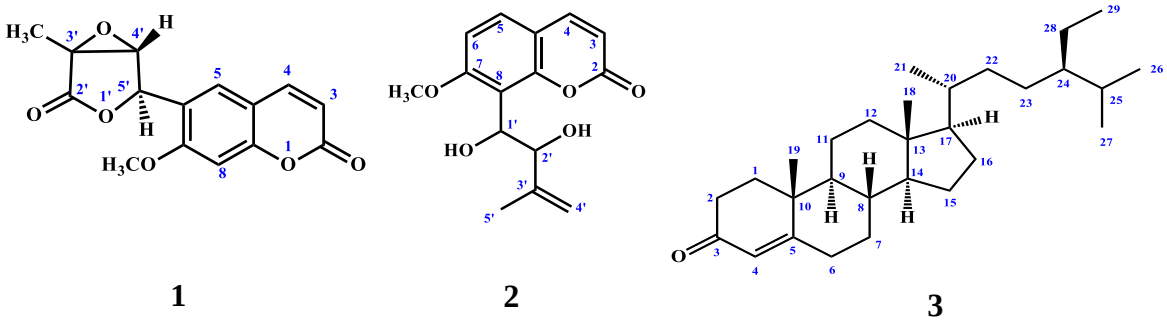

1 **2** **3**

Figure 1. Isolated compounds from the methanolic crude extract of the whole plant of *Micromelum minutum.*

3.1.1. Antioxidant activity.

Four different partitions of the methanolic extract of *M. minutum* were subjected to free radical scavenging activity [40]. It was observed that pet ether and chloroform fractions showed higher activity with IC_{50} values of 49.46 and 67.53 µg/mL, respectively, compared with the activity of BHT 31.02 µg/mL than that of other fractions. Carbon tetrachloride and aqueous fractions exhibited respectively very mild activity with IC_{50} values of 129.74 and 286.93 µg/mL (Figure 2).

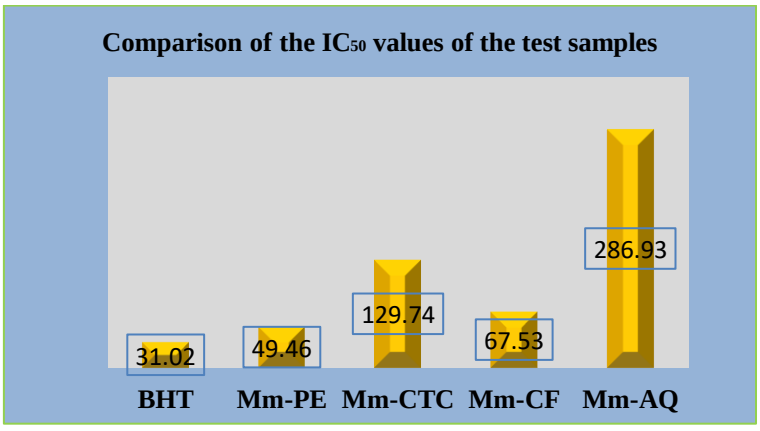

Figure 2. IC_{50} values of the standard and partitions of *Micromelum minutum.*

3.1.2. Cytotoxicity analysis.

The LC_{50} values obtained (Table 2) were 1.15, 5.14, 1.50, and 3.16 µg/mL for pet ether, carbon tetrachloride, chloroform, and aqueous fraction, respectively. The pet ether and chloroform fractions of *Micromelum minutum* showed good brine shrimp larvicidal activity

with LC_{50} values of 1.15 and 1.50 µg/mL respectively (Table 3) as compared to standard, vincristine sulfate (LC50 0.27 µg/mL) (Figure 3) [41].

Table 2. LC_{50} values of the test samples of whole plant of *Micromelum minutum.*

Sample code	Test samples	Regression line	R^2	LC_{50} (µg/mL)
VS	Vincristine Sulphate	y = 25.569x + 43.105	0.931	0.27
Mm-PE	Pet ether fraction	y = 30.401x + 15.077	0.9583	1.15
Mm-CTC	Carbon tetrachloride fraction	y = 7.4492x + 11.708	0.6012	5.14
Mm-CF	Chloroform fraction	y = 28.991x + 9.8354	0.9187	1.50
Mm-AQ	Aqueous fraction	y = 5.2346x + 33.47	0.5121	3.16

Table 3. Effect of pet ether, carbon tetrachloride, chloroform, and aqueous fractions of the methanolic extract on brine shrimp.

Conc. (mg/ml)	Log C		% mortality				LC_{50} (mg/mL)		
		Mm-PE	Mm-CTC	Mm-CF	Mm-AQ	Mm-PE	Mm-CTC	Mm-CF	Mm-AQ
400	2.602	100	20	100	50				
200	2.301	90	30	80	50				
100	2.000	70	30	60	40				
50	1.699	70	30	50	40				
25	1.398	50	30	40	40	1.15	5.14	1.50	3.16
12.5	1.097	40	20	40	30				
6.25	0.796	40	20	30	40				
3.13	0.495	30	10	30	40				
1.56	0.194	20	10	20	40				
0.78	-0.107	20	10	10	30				

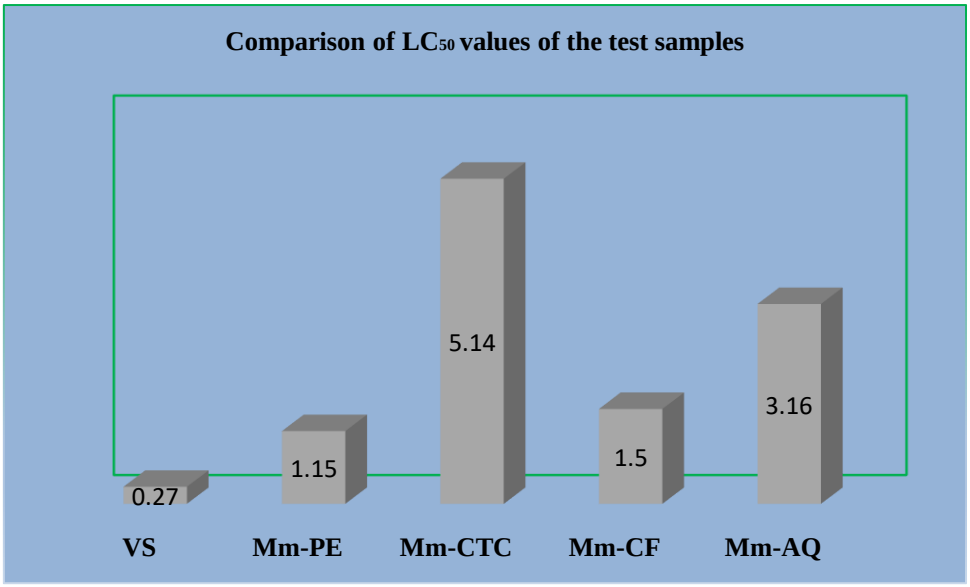

Figure 3. LC_{50} values of the test samples from *M. minutum.*

3.2. Computational analysis.

3.2.1 Molecular docking.

Molecular docking simulation is performed against SARS-CoV-2 M and N protein models (Figure 4 and 5) employing the desired phytochemical components from *Micromelum minutum* species [42]. The simulated interaction pattern and best binding poses of protein-

ligand complexes are illustrated by Auto Dock Vina [43]. Among the compounds, stigmast-4-en-3-one exerts the highest negative binding affinity (-9.1 kcal/mol) for interaction with SARS-CoV-2 M protein and develops a strong network with eleven hydrophobic bonds. Micromelin exposes binding affinity as -7.3 kcal/mol and is likely to be stabilized by two hydrogen bonds and eleven hydrophobic bonds. Murrangatin (binding affinity -6.8 kcal/mol) displays interactions with two hydrogen bonds and six hydrophobic bonds (Table 4). Stigmast-4-en-3-one and micromelin mostly interact with the residues of M protein interacting with S protein of SARS-CoV-2, whereas Murrangatin interacts with C terminal residues of M protein (Figure 6 and 7). For N protein, Stigmast-4-en-3-one compound provides the highest negative binding affinity (-8.6 kcal/mol) with the protein and renders stable interactions via two hydrogen bonds and eight hydrophobic bonds. Micromelin exhibits binding affinity as -8.5 kcal/mol and an established network with five hydrogen bonds and three hydrophobic bonds. Murrangatin (binding affinity -6.7 kcal/mol) promotes interactions with four hydrogen bonds, six hydrophobic bonds, and one electrostatic bond (Table 5). The compounds were interacting within the N-arm, a linker region, N-CTD dimerization and RNA binding domain, and C-tail regions of N protein (Figure 6 and 7). Hydrophobic bonds have played a significant role in protein-ligand interactions, contributing 88% in M protein and 59% in N protein for all interactions. Besides, hydrogen bonds have contributed by 38% and 12% in M and N proteins, respectively, while electrostatic interactions involve only in N protein by 3% of the total interactions (Figure 7E and 7F). After analyzing the interacting pattern, binding affinity, and best binding poses of the compounds, it can be suggested stigmast-4-en-3-one might be a promising candidate against SARS-CoV-2 M and N protein.

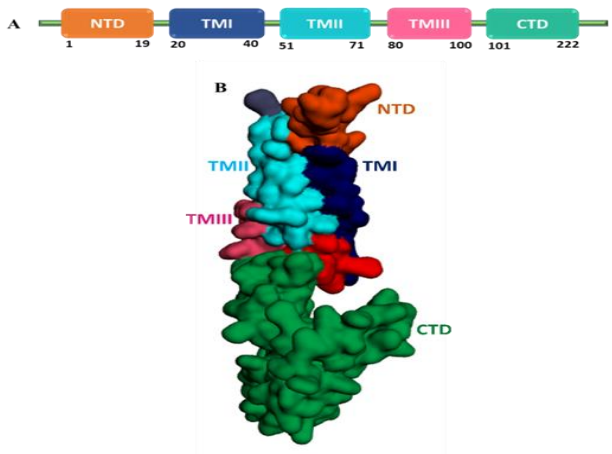

Figure 4. (A) Domains of SARS-CoV-2 M protein. Each domain is labeled with corresponding amino acids. **(B)** SARS-CoV-2 M model (trRosetta) protein with defined regions.

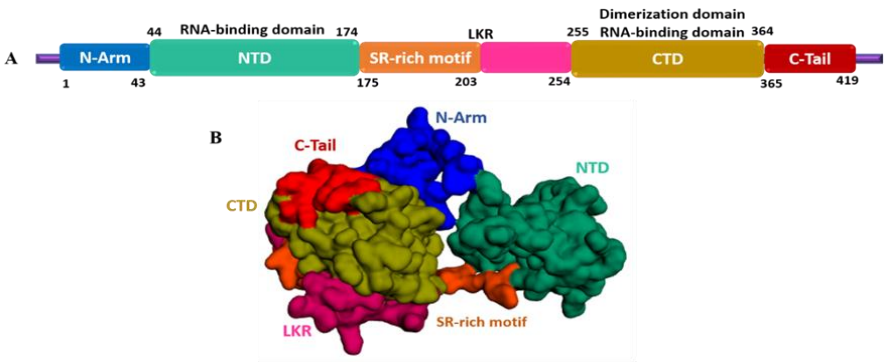

Figure 5. (A) Domains of SARS-CoV-2 N protein. Each domain is labeled with corresponding amino acids. **(B)** SARS-CoV-2 N model (I-TASSER) protein with defined regions.

Table 4. Non-covalent interactions of the compounds from *Micromelum minutum* species with SARS-CoV-2 M model (trRosetta) protein (Pose predicted by AutoDock Vina).

Compounds	Binding Affinity (kcal/mol)	Hydrophobic bond	Hydrogen bond	Electrostatic bond
Stigmast-4-en-3one	-9.1	Leu51, Trp55, Phe96, Phe100	_	_
		Phe103, Phe112		
Micromelin	-7.3	Trp55, Leu51, Trp92, Phe96, Phe100, Phe112	Trp92, Phe100	_
Murrangatin	-6.8	Val139, Val143, Tyr196	Gln185, Tyr196	_

Table 5. Non-covalent interactions of the top-ranked ligands from *Micromelum minutum* species with SARS-CoV-2 N model (I-TASSER) protein (Pose predicted by AutoDock Vina).

Compounds	Binding Affinity (kcal/mol)	Hydrophobic bond	Hydrogen bond	Electrostatic bond
Stigmast-4-en-3one	-8.6	Leu221, Leu224, Leu353, Ile357, Leu394, Leu395	Gly5, Gly25	_
Micromelin	-8.5	Arg10, Gly19, Gln281, Thr393	Pro6, Leu395	_
Murrangatin	-6.7	Leu394, Leu395, Leu407	Ser2, Ser23, Thr393, Leu394	Arg10

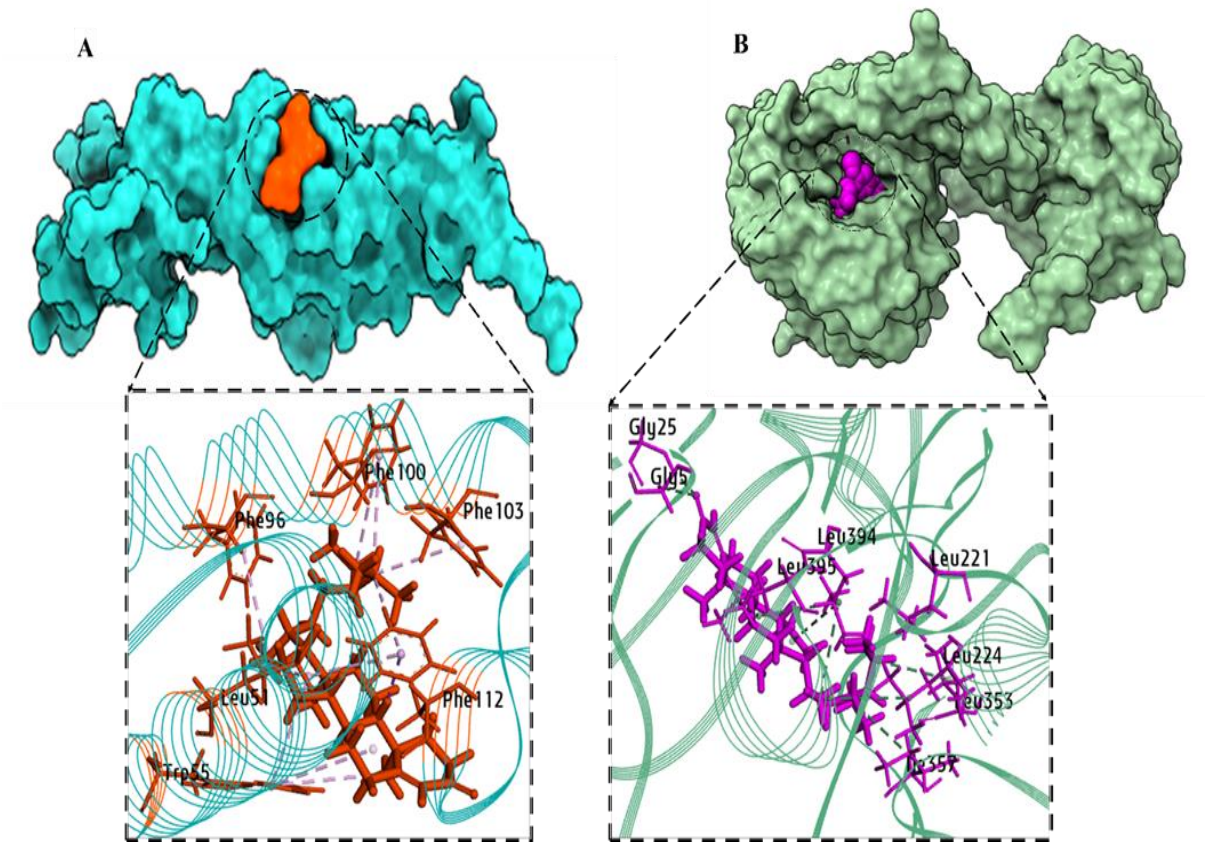

Figure 6. Non-covalent interactions of Stigmast-4-en-3-one with **(A)** SARS-CoV-2 M and **(B)** N model proteins (Pose predicted by AutoDock Vina).

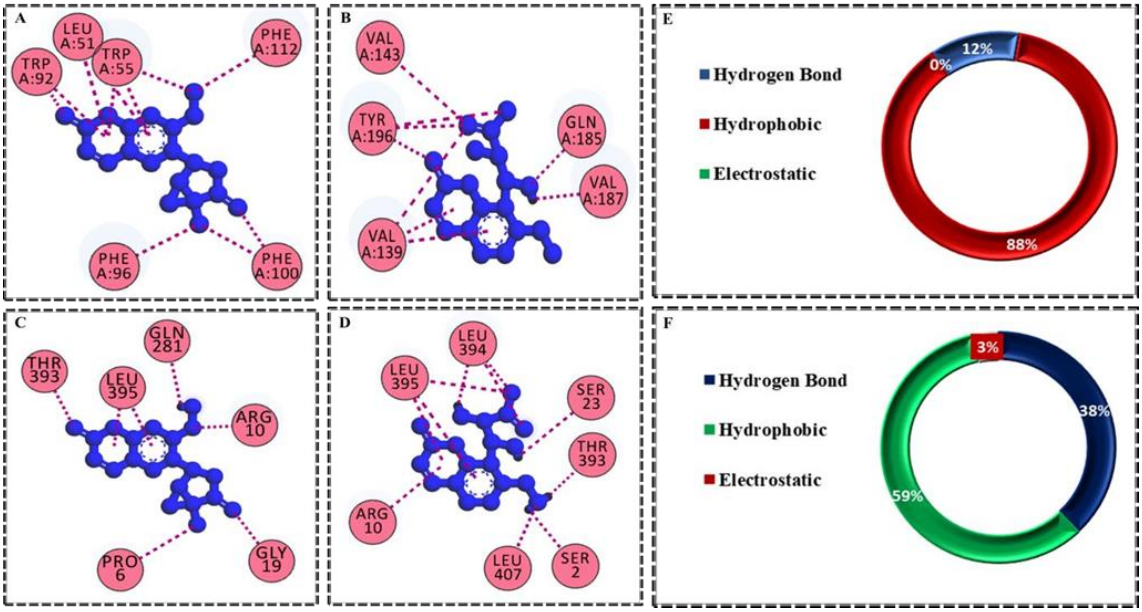

Figure 7. Non-covalent interactions of Micromelin and Murrangatin with **(A, B)** SARS-CoV-2 M and **(C, D)** N model proteins (Pose predicted by AutoDock Vina), **(E, F)** Distribution of non-covalent interactions M and N model proteins, respectively.

3.2.2 Analysis of ADMET studies

ADMET profiles of the selected compounds are recorded in (Table 6**)** [44, 45]. The probable success rate of small therapeutic molecules is determined by pharmacokinetic and toxicity properties. In this work, the ADMET study emphasizes solubility (LogS), human intestinal absorption (HIA), CaCO-2 permeability, P-glycoprotein substrate inhibition, cytochrome inhibitor, AMES toxicity, max. tolerated dose (human), and hepatotoxicity. The selected compounds exhibit optimum solubility. The selected inhibitors show notable human intestinal absorption (HIA); high Caco2 permeability indicates high absorption in the intestine upon oral administration. In terms of distribution, stigmast-4-en-3-one and micromelin possess better CNS permeability than murrangatin. All compounds are found to be non-inhibitor of cytochrome P450 (CYP 450), demonstrating their appropriate metabolism by CYP 450. Besides, the compounds are non-inhibitor of human Ether-ago-go-Related Gene (hERG), phosphorylated glycoprotein (P-gp), and non-hepatotoxic. However, micromelin is predicted as AMES toxic. Max. tolerated dose (human) level of stigmast-4-en-3-one is lower (-0.54) than micromelin (0.173) and murrangatin (0.559). The values indicate the recommended starting dose of the compounds in phase I clinical trials.

Table 6. ADMET properties of the compounds.

Ligands	MF	molMW	Log S	HIA	Caco-2 (cm/s)	CNS	hERG	PGI	CYP450 2D6/3	AMES toxicity	HMTD	Hepatotoxicity
Compound **3**	C29H48O	412.69	-6.108	96.944	1.206	-1.324	No	No	No	No	-0.54	No
Compound **1**	C15H12O6	288.25	-2.877	100	1.432	-2.993	No	No	No	Yes	0.173	Yes
Compound **2**	C15H16O5	276.28	-2.833	96.623	1.123	-3.266	No	No	No	No	0.559	No

MF- Molecular formula HIA- Human intestinal absorption; CNS- Central Nervous System; hERG- the human Ether-a-go-go-Related Gene; PGI- P-glycoprotein inhibitor, HMTD- Human Max. tolerated dose

3.2.3. Molecular dynamics simulation.

MD simulation for apo M, N proteins and their complexes with stigmast-4-en-3-one are performed for 50 ns. The RMSDs (0.734–15.775 Å) for α-carbon atoms (average 12.87 Å) in apo-M protein (highest peak at 16.5 ns) is much higher than its complex with the compound (average 5.2 Å), thus suggesting that M protein complex remains more stable in the whole simulation (Figure 8A). For N protein, the RMSDs (1.378–9.82 Å) for α-carbon atoms in apo-N protein is also higher than the complex (1.365-7.845 Å). However, several overlapping trends have been observed between 0-30 ns in both apo and the complex. Later, apoprotein significantly deviates more than the complex till the end, conferring that the bound form of the protein is likely to be stable in physiological conditions (Figure 8C).

RMSF values are also calculated to determine the residual dynamics of both proteins. In the case of M protein, the RMSF of residues in N-terminal and transmembrane domains exhibits a quite similar pattern in both apo and the complex. However, the residues (101-222) in C-terminal flanking tail significantly fluctuate in apoprotein than the protein-ligand complex (Figure 8B). Here, less fluctuation in protein-ligand complex indicates higher structural stability. Thus, it reflects that crucial interacting residues Leu51, Trp55, Phe96, Phe100, Phe103, and Phe112 remained more stable to stimulate strong interactions with stigmast-4en-3-one. For N protein, RMSF values of apoprotein follow a rising trend than protein-ligand complex except at 43, 237, and 312 residues. The minimal fluctuation in almost the whole complex renders more stability during simulation. Hence, the key residues Gly5, Gly25, Leu221, Leu224, Leu353, Ile357, Leu394, and Leu395 of N protein provide stable interactions with stigmast-4-en-3-one compound (Figure 8D). MD simulations support the docking results demonstrating that stigmast-4-en-3-one can effectively interact with M and N proteins.

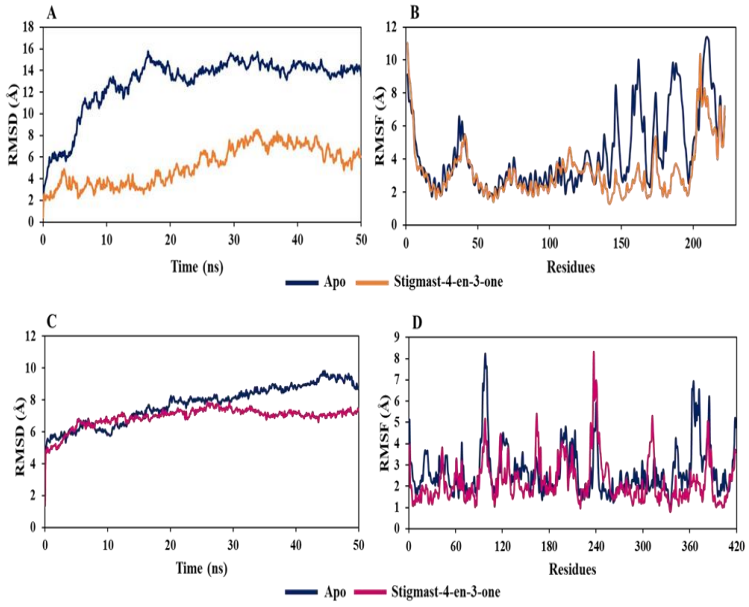

Figure 8. RMSD and RMSF values of **(A, B)** SARS-CoV-2 M and **(C, D)** N model proteins for apoproteins and complexes with the selected compound during MD simulation.

In this study, we have employed integrated computational methods to screen three phytochemical components from *Micromelum minutum* species to identify potential candidates against the M and N protein of SARS-CoV-2. Here, *in silico* approaches assist in narrowing down the synthetic and biological testing efforts. The findings will be helpful to test the efficacy of the stigmast-4-en-3-one compound through *in vitro* and *in vivo* settings against SARS-CoV-2. The interacting regions are crucial for screening and developing antiviral inhibitors against SARS-CoV-2 [5].

4. Conclusions

The present study identified two coumarins (**1**, **2**) and one sterol (**3**) from the crude extracts of *M. minutum*, of which (**3**) are reported herein for the first time from this plant. During viral replication and assembly, the structural proteins play a crucial role in associating viral particles. Here, we have screened three phytochemical components from *Micromelum minutum* species to distinguish the potentiality of drug candidates against the M and N protein of SARS-CoV-2. The docking simulation shows that stigmast-4-en-3-one (**3**) might be an effective compound against M and N protein to interact with their crucial residues. MD simulations support the docking results signifying that stigmast-4-en-3-one can effectively interact with both M and N proteins. The outcomes will support investigating the effectiveness of the stigmast-4-en-3-one compound through *in vitro* and *in vivo* trials against SARS-CoV-2. The identified interactions are indispensable for the screening and developing antiviral inhibitors against SARS-CoV-2. ADMET analysis demonstrates that stigmast-4-en-3-one is non-carcinogenic with comparatively good human intestinal absorption, CNS penetration probability, and no inhibition of cytochrome P450 (CYP 450), signifying their appropriate metabolism by CYP 450.

Funding

This research received no external funding.

Acknowledgments

We thank Mohammad A. Halim, Assistant Professor, Department of Physical Sciences, University of Arkansas - Fort Smit (Division of Infectious Diseases and Division of Computer-Aided Drug Design, The Red-Green Research Centre, BICCB, Tejgaon, Dhaka, Bangladesh), for the suggestions and support of the computational facilities to perform MD simulation

Conflicts of Interest

The authors declare no conflict of interest.

References

1. Hasöksüz, M.; Kiliç, S.; Saraç, F. Coronaviruses and sars-cov-2. *Turkish journal of medical sciences* **2020,** *50*, 549-556, https://doi.org/10.3906/sag-2004-127.
2. Gordon, D. E.; Jang, G. M.; Bouhaddou, M.; Xu, J.; Obernier, K.; White, K. M.; O'Meara, M. J.; Rezelj, V. V.; Guo, J. Z.; Swaney, D. L. A SARS-CoV-2 protein interaction map reveals targets for drug repurposing. *Nature* **2020,** *583*, 459-468, https://doi.org/10.1038/s41586-020-2286-9.
3. Li, H.; Zhou, Y.; Zhang, M.; Wang, H.; Zhao, Q.; Liu, J. Updated approaches against SARS-CoV-2. *Antimicrobial agents and chemotherapy* **2020,** *64*, e00483-20, https://doi.org/10.1128/aac.00483-20.
4. Li, J.; Guo, M.; Tian, X.; Wang, X.; Yang, X.; Wu, P.; Liu, C.; Xiao, Z.; Qu, Y.; Yin, Y. Virus-host interactome and proteomic survey reveal potential virulence factors influencing SARS-CoV-2 pathogenesis. *Med* **2021,** *2*, 99-112. e7, https://doi.org/10.1016/j.medj.2020.07.002.
5. Peng, Y.; Du, N.; Lei, Y.; Dorje, S.; Qi, J.; Luo, T.; Gao, G. F.; Song, H. Structures of the SARS-CoV-2 nucleocapsid and their perspectives for drug design. *Embo j* **2020,** *39*, e105938, https://doi.org/10.15252/embj.2020105938.
6. Bhowmik, D.; Nandi, R.; Jagadeesan, R.; Kumar, N.; Prakash, A.; Kumar, D. Identification of potential inhibitors against SARS-CoV-2 by targeting proteins responsible for envelope formation and virion assembly

using docking based virtual screening, and pharmacokinetics approaches. *Infection, Genetics and Evolution* **2020,** *84*, 104451, https://doi.org/10.1016/j.meegid.2020.104451.
7. Xu, R.; Shi, M.; Li, J.; Song, P.; Li, N. Construction of SARS-CoV-2 virus-like particles by mammalian expression system. *Frontiers in bioengineering and biotechnology* **2020,** *8*, 862, http://dx.doi.org/10.3389/fbioe.2020.00862.
8. Zhang, X.; Liu, Y.; Liu, J.; Bailey, A. L.; Plante, K. S.; Plante, J. A.; Zou, J.; Xia, H.; Bopp, N. E.; Aguilar, P. V. A trans-complementation system for SARS-CoV-2 recapitulates authentic viral replication without virulence. *Cell* **2021,** *184* (8), 2229-2238. e13, https://doi.org/10.1016/j.cell.2021.02.044.
9. Schoeman, D.; Fielding, B. C. Coronavirus envelope protein: current knowledge. *Virology journal* **2019,** *16*, 1-22, https://doi.org/10.1186/s12985-019-1182-0.
10. Mahtarin, R.; Islam, S.; Islam, M. J.; Ullah, M. O.; Ali, M. A.; Halim, M. A. Structure and dynamics of membrane protein in SARS-CoV-2. *Journal of Biomolecular Structure and Dynamics* **2020**, 1-14, https://doi.org/10.1080/07391102.2020.1861983.
11. Ray, M.; Sarkar, S.; Rath, S. N. Druggability for COVID-19: in silico discovery of potential drug compounds against nucleocapsid (N) protein of SARS-CoV-2. *Genomics & Informatics* **2020,** *18*, e43, https://doi.org/10.5808/gi.2020.18.4.e43.
12. Kang, S.; Yang, M.; Hong, Z.; Zhang, L.; Huang, Z.; Chen, X.; He, S.; Zhou, Z.; Zhou, Z.; Chen, Q. Crystal structure of SARS-CoV-2 nucleocapsid protein RNA binding domain reveals potential unique drug targeting sites. *Organization* **2020,** *12*, 1, https://doi.org/10.1016/j.apsb.2020.04.009.
13. Lekphrom, R.; Kanokmedhakul, S.; Kukongviriyapan, V.; Kanokmedhakul, K. C-7 oxygenated coumarins from the fruits of Micromelum minutum. *Archives of pharmacal research* **2011,** *34*, 527-531, https://doi.org/10.1007/s12272-011-0402-y.
14. Khan, M. F.; Rabbi, S. N. I.; Aktar, F. Kawsar, M. H. In vitro cytotoxic, membrane stabilizing and thrombolytic activities of Polygonum glabrum Willd. *Bangladesh Pharmaceutical Journal* **2014,** *17*, 202-204, https://doi.org/10.3329/bpj.v17i2.22341.
15. Brand-Williams, W.; Cuvelier, M.-E.; Berset, C. Use of a free radical method to evaluate antioxidant activity. *LWT-Food science and Technology* **1995,** *28*, 25-30, https://doi.org/10.1016/S0023-6438(95)80008-5.
16. Asmah Susidarti, R.; Rahmani, M.; Ismail, H. B.; Sukari, M. A.; Yun Hin, T.-Y.; Ee Cheng Lian, G.; Manaf Ali, A. Cytotoxic activity of coumarins from Micromelum minutum. *Pharmaceutical Biology* **2009,** *47*, 182-185, http://dx.doi.org/10.1080/13880200802436513.
17. Wagner, F.; Becker, G.; Behringer, K.; Campbell, D.; Eberhagen, A.; Engelhardt, W.; Fussmann, G.; Gehre, O.; Gernhardt, J.; Gierke, G. v. Regime of improved confinement and high beta in neutral-beam-heated divertor discharges of the ASDEX tokamak. *Physical Review Letters* **1982,** *49*, 1408, https://doi.org/10.1103/PhysRevLett.49.1408.
18. Sousa, S. F.; Fernandes, P. A.; Ramos, M. J. Protein–ligand docking: current status and future challenges. *Proteins: Structure, Function, and Bioinformatics* **2006,** *65*, 15-26, https://doi.org/10.1002/prot.21082.
19. Calligari, P.; Bobone, S.; Ricci, G.; Bocedi, A. Molecular investigation of SARS–CoV-2 proteins and their interactions with antiviral drugs. *Viruses* **2020,** *12*, 445, https://doi.org/10.3390/v12040445.
20. Yang, J.; Anishchenko, I.; Park, H.; Peng, Z.; Ovchinnikov, S.; Baker, D. Improved protein structure prediction using predicted interresidue orientations. *Proceedings of the National Academy of Sciences* **2020,** *117* , 1496-1503, https://doi.org/10.1073/pnas.1914677117.
21. Bazzoli, A.; Tettamanzi, A. G.; Zhang, Y. Computational protein design and large-scale assessment by I-TASSER structure assembly simulations. *Journal of molecular biology* **2011,** *407*, 764-776, https://dx.doi.org/10.1016%2Fj.jmb.2011.02.017.
22. Christenholz, C. L.; Obenchain, D. A.; Peebles, R. A.; Peebles, S. A. Rotational spectroscopic studies of C–H⋯ F interactions in the vinyl fluoride⋯ difluoromethane complex. *The Journal of Physical Chemistry A* **2014,** *118*, 1610-1616, https://doi.org/10.1021/jp500312r.
23. Bikadi, Z.; Hazai, E. Application of the PM6 semi-empirical method to modeling proteins enhances docking accuracy of AutoDock. *Journal of cheminformatics* **2009,** *1*, 1-16, https://doi.org/10.1186/1758-2946-1-15.
24. Nguyen, N. T.; Nguyen, T. H.; Pham, T. N. H.; Huy, N. T.; Bay, M. V.; Pham, M. Q.; Nam, P. C.; Vu, V. V.; Ngo, S. T. Autodock vina adopts more accurate binding poses but autodock4 forms better binding affinity. *Journal of Chemical Information and Modeling* **2019,** *60*, 204-211, https://doi.org/10.1021/acs.jcim.9b00778.

25. Ahmed, S.; Mahtarin, R.; Islam, M. S.; Das, S.; Al Mamun, A.; Ahmed, S. S.; Ali, M. A. Remdesivir analogs against SARS-CoV-2 RNA-dependent RNA polymerase. *Journal of Biomolecular Structure and Dynamics* **2021**, 1-14, https://doi.org/10.1080/07391102.2021.1955743.
26. Ahmed, S.; Mahtarin, R.; Ahmed, S. S.; Akter, S.; Islam, M. S.; Mamun, A. A.; Islam, R.; Hossain, M. N.; Ali, M. A.; Sultana, M. U. Investigating the binding affinity, interaction, and structure-activity-relationship of 76 prescription antiviral drugs targeting RdRp and Mpro of SARS-CoV-2. *Journal of Biomolecular Structure and Dynamics* **2020**, 1-16, https://doi.org/10.1080/07391102.2020.1796804.
27. Ahmed, S.; Islam, N.; Shahinozzaman, M.; Fakayode, S. O.; Afrin, N.; Halim, M. A. Virtual screening, molecular dynamics, density functional theory and quantitative structure activity relationship studies to design peroxisome proliferator-activated receptor-γ agonists as anti-diabetic drugs. *Journal of Biomolecular Structure and Dynamics* **2021,** *39*, 728-742, https://doi.org/10.1080/07391102.2020.1714482.
28. Zahan, R.; Ahmed, S.; Sharmin, T.; Halim, M. A.; Rahi, M. S.; Sheikh, M. C.; Miyatake, R.; Zangrando, E.; Naz, T.; Islam, M. A. A. A. A. Synthesis of bis [benzyl-N′-hydrazinecarbodithioato-κ2 N′, S] nickel (II) complex as a novel lead molecule for cancer treatment. *Applied Organometallic Chemistry* **2021,** *35*, e6036, https://doi.org/10.1002/aoc.6036.
29. Pires, D. E.; Blundell, T. L.; Ascher, D. B., pkCSM: predicting small-molecule pharmacokinetic and toxicity properties using graph-based signatures. *Journal of medicinal chemistry* **2015,** *58*, 4066-4072, https://doi.org/10.1021/acs.jmedchem.5b00104.
30. Capecchi, A.; Awale, M.; Probst, D.; Reymond, J. L., PubChem and CHEMBL beyond Lipinski. *Molecular informatics* **2019,** *38*, 1900016, https://doi.org/10.1002/minf.201900016.
31. Susnow, R. G.; Dixon, S. L. Use of robust classification techniques for the prediction of human cytochrome P450 2D6 inhibition. *J Chem Inf Comput Sci* **2003,** *43*, 1308-15, https://doi.org/10.1021/ci030283p.
32. Krieger, E.; Darden, T.; Nabuurs, S. B.; Finkelstein, A.; Vriend, G. Making optimal use of empirical energy functions: force-field parameterization in crystal space. *Proteins: Structure, Function, and Bioinformatics* **2004,** *57*, 678-683, https://doi.org/10.1002/prot.20251.
33. Krieger, E.; Vriend, G. New ways to boost molecular dynamics simulations. *Journal of computational chemistry* **2015,** *36*, 996-1007, https://doi.org/10.1002/jcc.23899.
34. Lemak, A.; Balabaev, N., On the Berendsen thermostat. *Molecular Simulation* **1994,** *13*, 177-187, https://doi.org/10.1080/08927029408021981.
35. Lamberton, J. A.; Price, J.; Redcliffe, A. Micromelin, a new coumarin from Micromelum minutum (Forst. f.) Seem (family Rutaceae). *Australian Journal of Chemistry* **1967,** *20*, 973-979, https://doi.org/10.1071/CH9670973.
36. Tantivatana, P.; Ruangrungsi, N.; Vaisiriroj, V.; Lankin, D. C.; Bhacca, N. S.; Borris, R. P.; Cordell, G. A.; Johnson, L. F. Microminutin, a novel cytotoxic coumarin from Micromelum minutum (Rutaceae). *The Journal of Organic Chemistry* **1983,** *48*, 268-270, https://doi.org/10.1021/jo00150a028.
37. Rahmani, M.; Susidarti, R. A.; Ismail, H. B.; Sukari, M. A.; Hin, T.-Y. Y.; Lian, G. E. C.; Ali, A. M.; Kulip, J.; Waterman, P. G. Coumarins from Malaysian Micromelum minutum. *Phytochemistry* **2003,** *64*, 873-877, https://doi.org/10.1016/j.phytochem.2003.08.007.
38. Rahmani, M.; Taufiq-Yap, Y. H.; Ismail, H. B.; Sukari, A.; Waterman, P. G. New coumarin and dihydrocinnamic acid derivatives from two Malaysian populations of Micromelum minutum. *Phytochemistry* **1994,** *37*, 561-564, https://doi.org/10.1016/0031-9422(94)85100-X.
39. Muhammed, M. T.; Aki-Yalcin, E. Homology modeling in drug discovery: Overview, current applications, and future perspectives. *Chemical biology & drug design* **2019,** *93*, 12-20, https://doi.org/10.1111/cbdd.13388.
40. Kassim, N. K.; Lim, P. C.; Ismail, A.; Awang, K. Isolation of antioxidative compounds from Micromelum minutum guided by preparative thin layer chromatography-2, 2-diphenyl-1-picrylhydrazyl (PTLC-DPPH) bioautography method. *Food chemistry* **2019,** *272*, 185-191, https://doi.org/10.1016/j.foodchem.2018.08.045.
41. Susidarti, R. A.; Meiyanto, E.; Ikawati, M.; Sida, N. A. Indonesian Micromelum minutum Leave Extracts and Their Cytotoxic Activities Toward Breast Cancer Cell Lines. *Journal of Mathematical & Fundamental Sciences* **2021,** *53*, https://repo-dosen.ulm.ac.id//handle/123456789/21090.
42. Thant, T. M.; Aminah, N. S.; Kristanti, A. N.; Ramadhan, R.; Aung, H. T.; Takaya, Y. Phytoconstituents of Genus Micromelum and Their Bioactivity—a Review. *Natural Product Communications* **2020,** *15*, 1934578X20927124, https://doi.org/10.1177%2F1934578X20927124.

43. Trott, O.; Olson, A. J. AutoDock Vina: improving the speed and accuracy of docking with a new scoring function, efficient optimization, and multithreading. *Journal of computational chemistry* **2010,** *31*, 455-461, https://doi.org/10.1002/jcc.21334.
44. Ferreira, L. L.; Andricopulo, A. D. ADMET modeling approaches in drug discovery. *Drug discovery today* **2019,** *24*, 1157-1165, https://doi.org/10.1016/j.drudis.2019.03.015.
45. Norinder, U.; Bergström, C. A. Prediction of ADMET properties. *Chem Med Chem: Chemistry Enabling Drug Discovery* **2006,** *1*, 920-937, https://doi.org/10.1002/cmdc.200600155.

Supplementary files

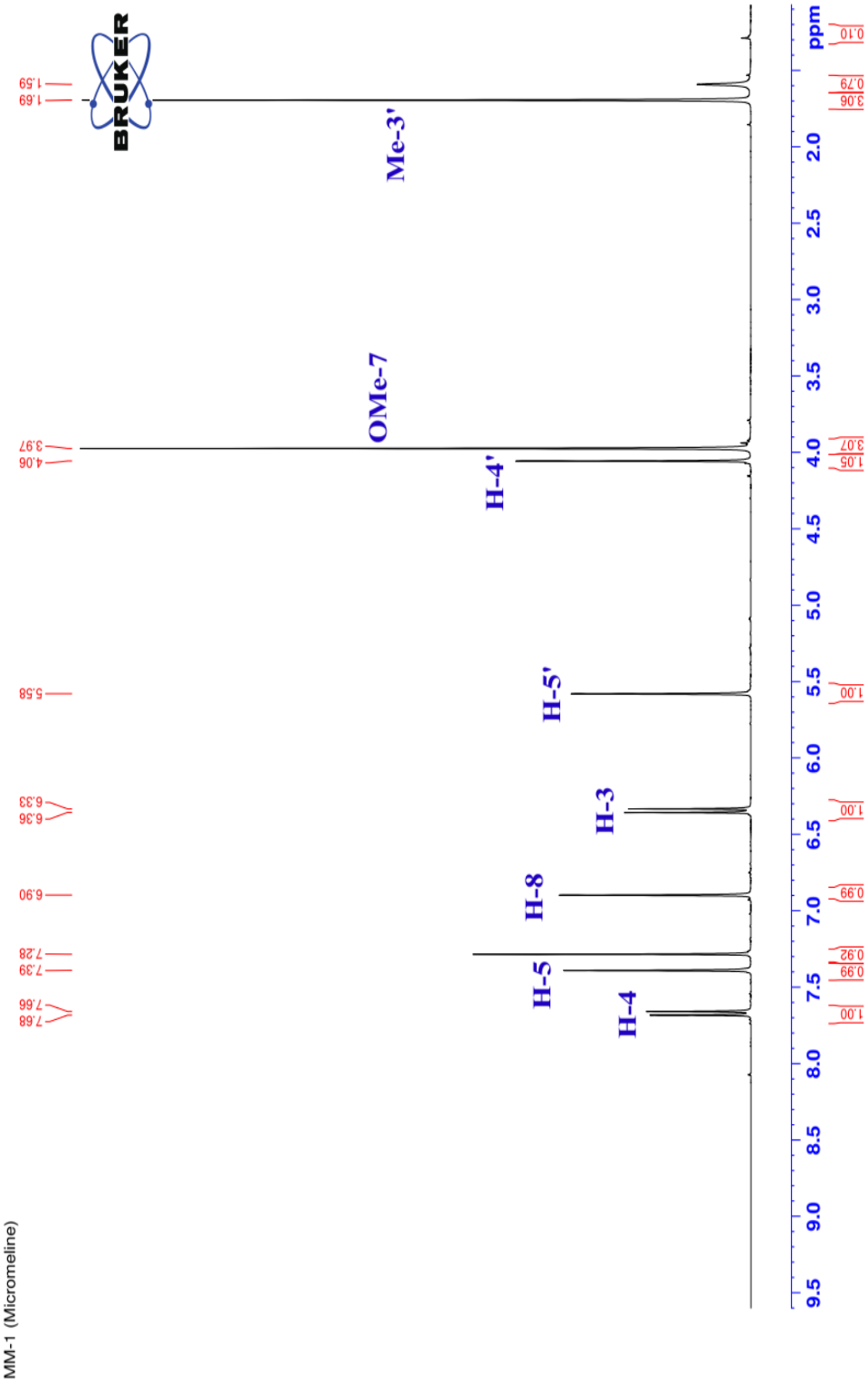

Figure S9. ^{1}H NMR (400 MHz, $CDCl_3$) spectrum of compound 1 (MM-1)

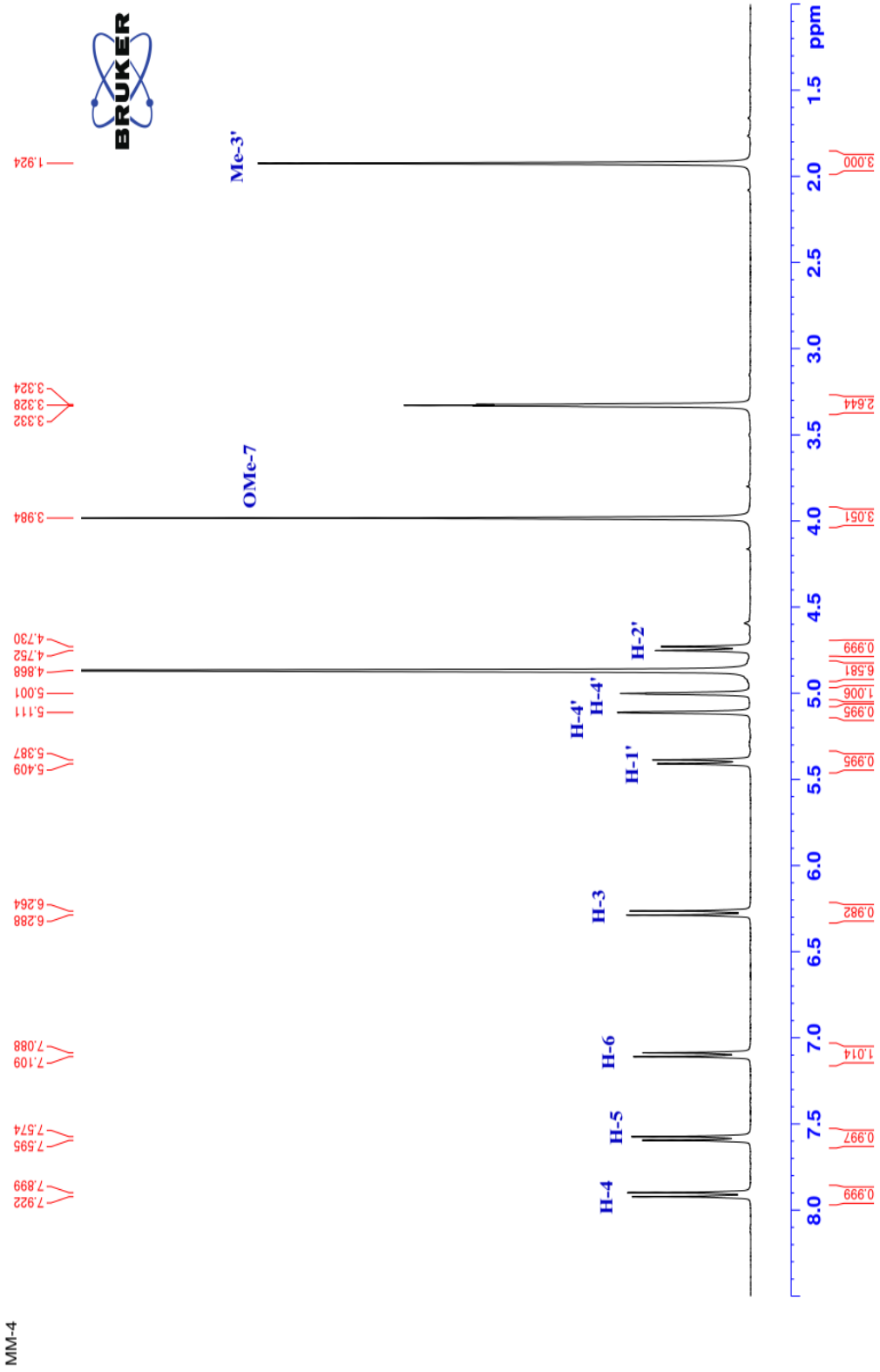

Figure S10. ^{1}H NMR (400 MHz, $CDCl_3$) spectrum of compound 2 (MM-4)

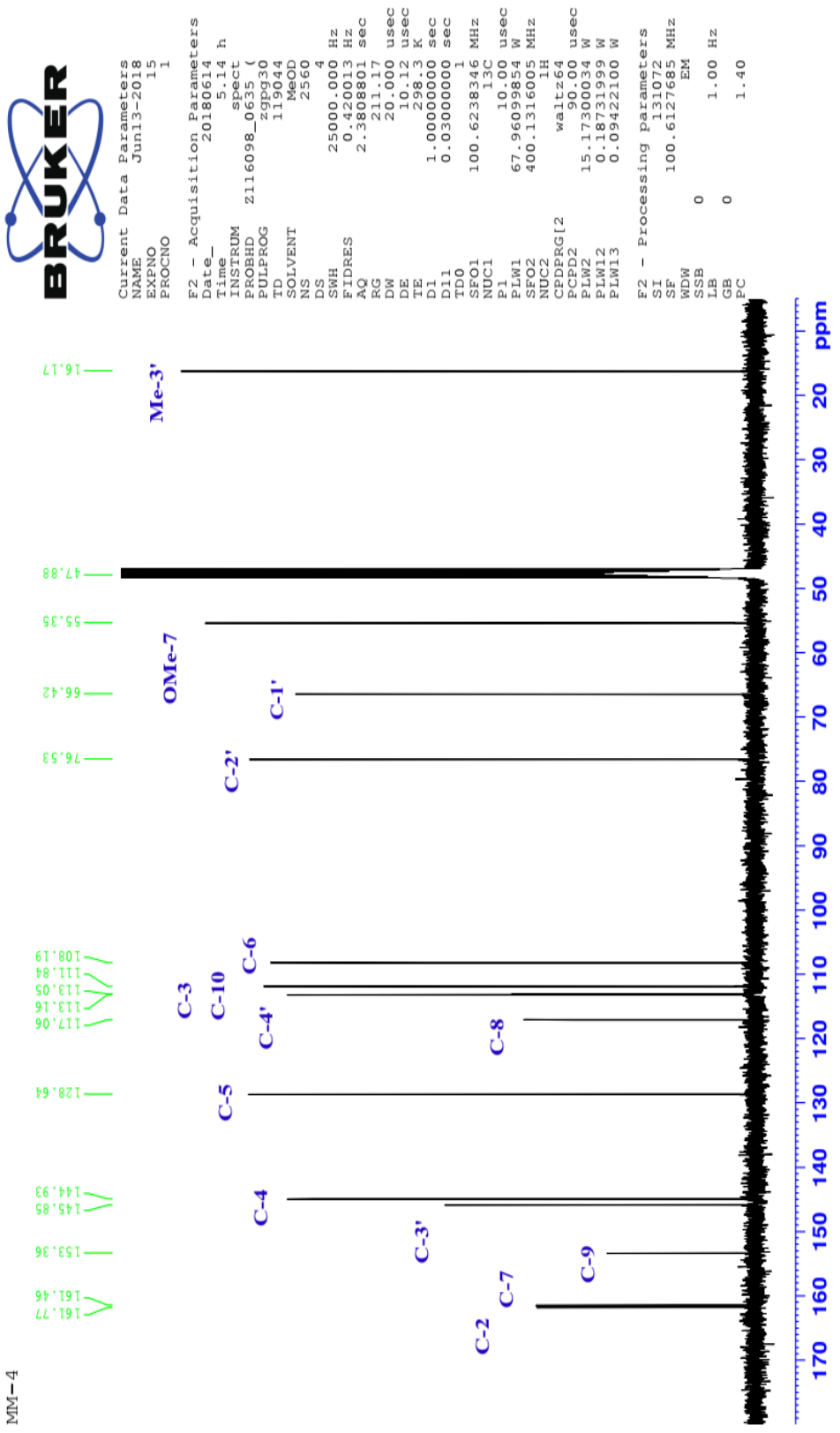

Figure S10.2. COSY (400 MHz, $CDCl_3$) spectrum of compound 2 (MM-4)

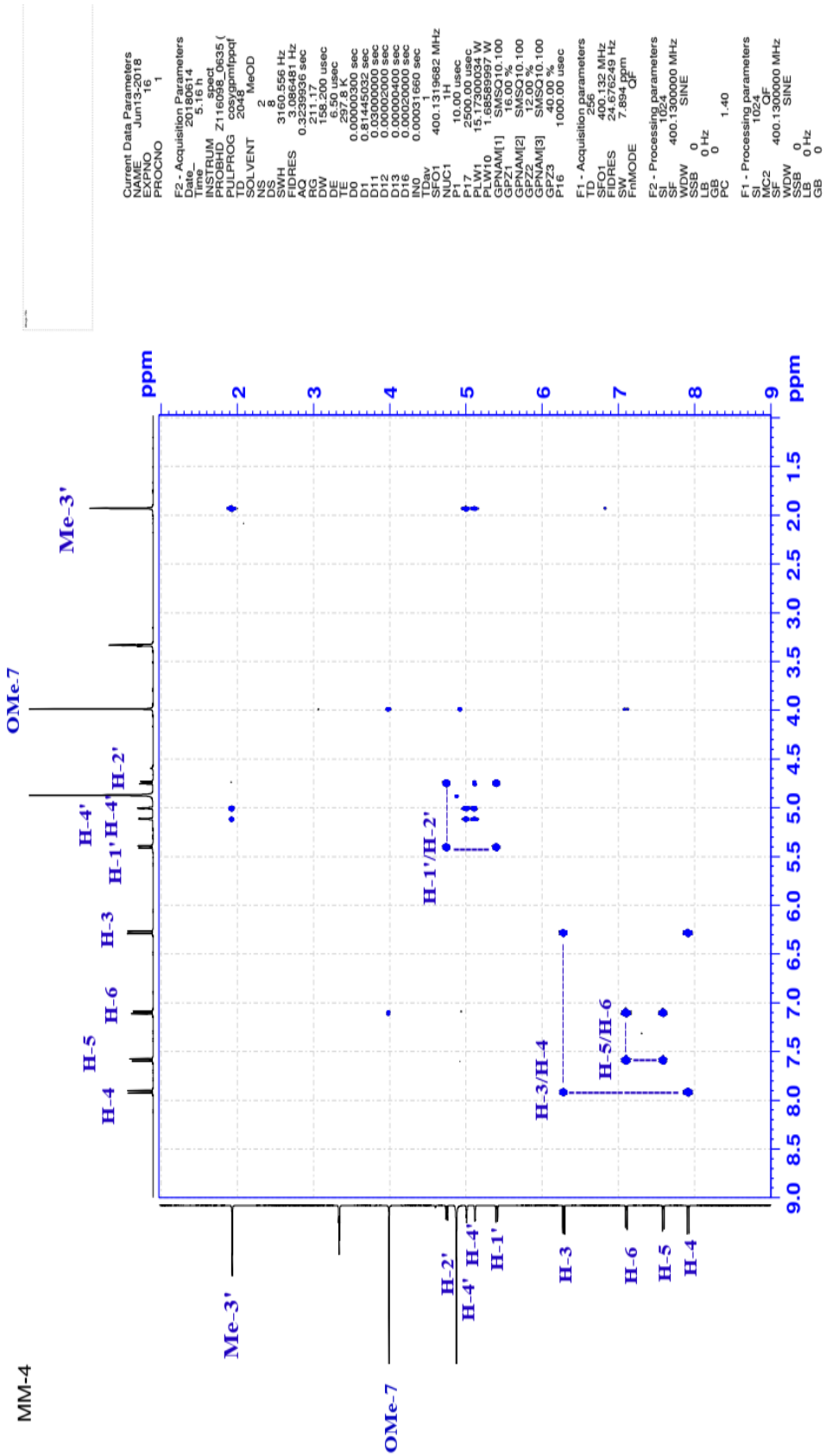
Current Data Parameters
NAME MM-4
EXPNO 16
PROCNO 1
F2 - Acquisition Parameters
Date_ 20180614
Time 5.16 h
INSTRUM spect
PROBHD Z116098_0635 (
PULPROG cosygpmfppqf
TD 2048
SOLVENT MeOD
NS 2
DS 8
SWH 3160.556 Hz
FIDRES 3.086481 Hz
AQ 0.3239936 sec
RG 214.17
DW 158.200 usec
DE 6.50 usec
TE 297.8 K
D0 0.00000300 sec
D1 0.81445032 sec
D11 0.03000000 sec
D12 0.00002000 sec
D13 0.00000400 sec
D16 0.00020000 sec
IN0 0.00031660 sec
TDav 1
SFO1 400.1319682 MHz
NUC1 1H
P1 10.00 usec
P17 2500.00 usec
PLW1 15.17300034 W
PLW10 1.68589997 W
GPNAM[1] SMSQ10.100
GPZ1 16.00 %
GPNAM[2] SMSQ10.100
GPZ2 17.00 %
GPNAM[3] SMSQ10.100
GP23 40.00 %
P16 1000.00 usec
F1 - Acquisition parameters
TD 256
SFO1 400.132 MHz
FIDRES 24.676249 Hz
SW 7.894 ppm
FnMODE QF
F2 - Processing parameters
SI 1024
SF 400.1300000 MHz
WDW SINE
SSB 0
LB 0 Hz
GB 0
PC 1.40
F1 - Processing parameters
SI 1024
MC2 QF
SF 400.1300000 MHz
WDW SINE
SSB 0
LB 0 Hz
GB 0
ppm
Me-3'
OMe-7
H-4'
H-1'/H-4'
H-2'
H-3
H-6
H-5
H-4
H-1'/H-2'
H-3/H-4
H-5/H-6
MM-4
OMe-7
Me-3'
H-2'
H-4'
H-1'
H-3
H-6
H-5
H-4

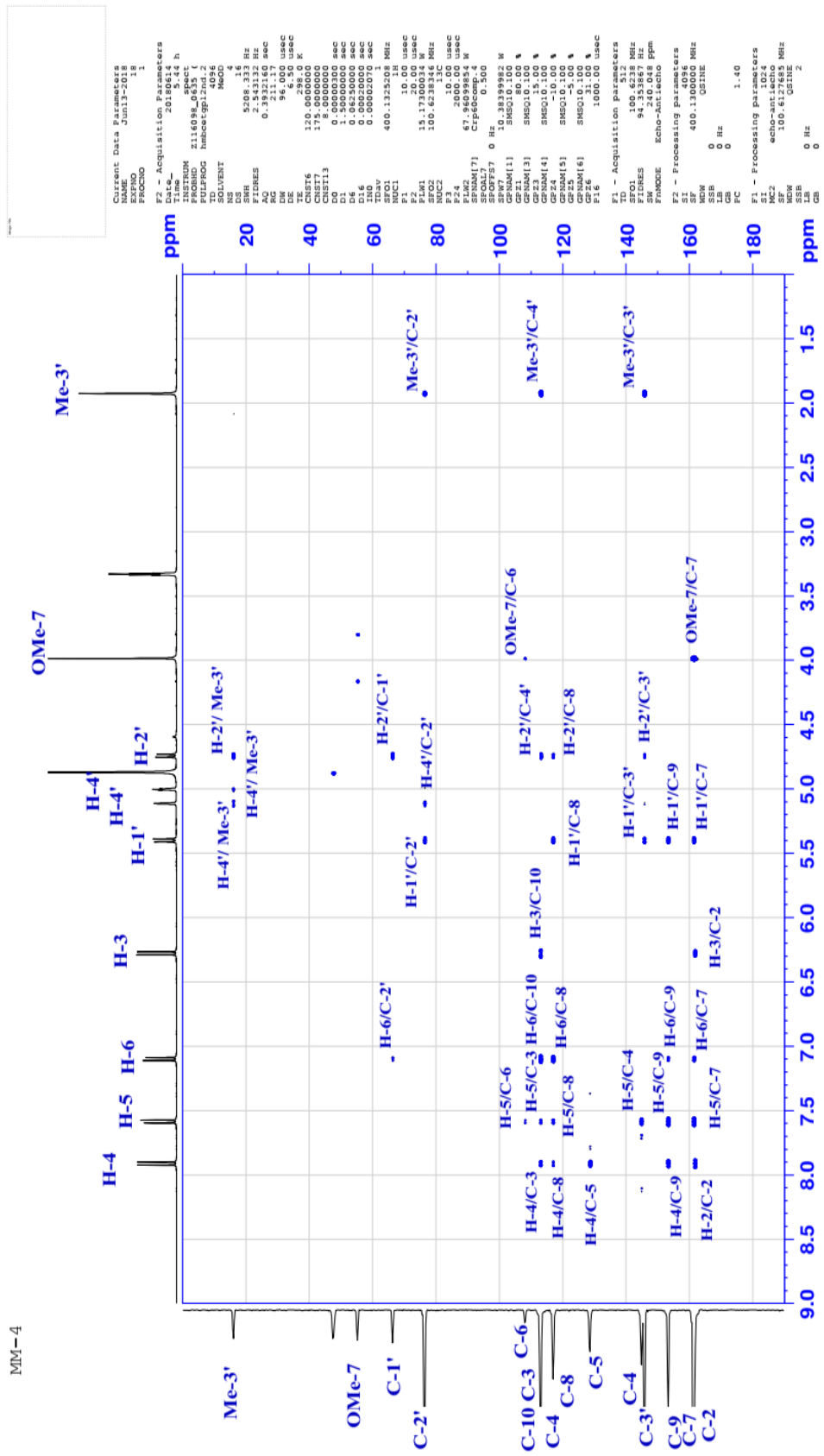

Figure S10.3. HMBC (400 MHz, $CDCl_3$) spectrum of compound 2 (MM-4)

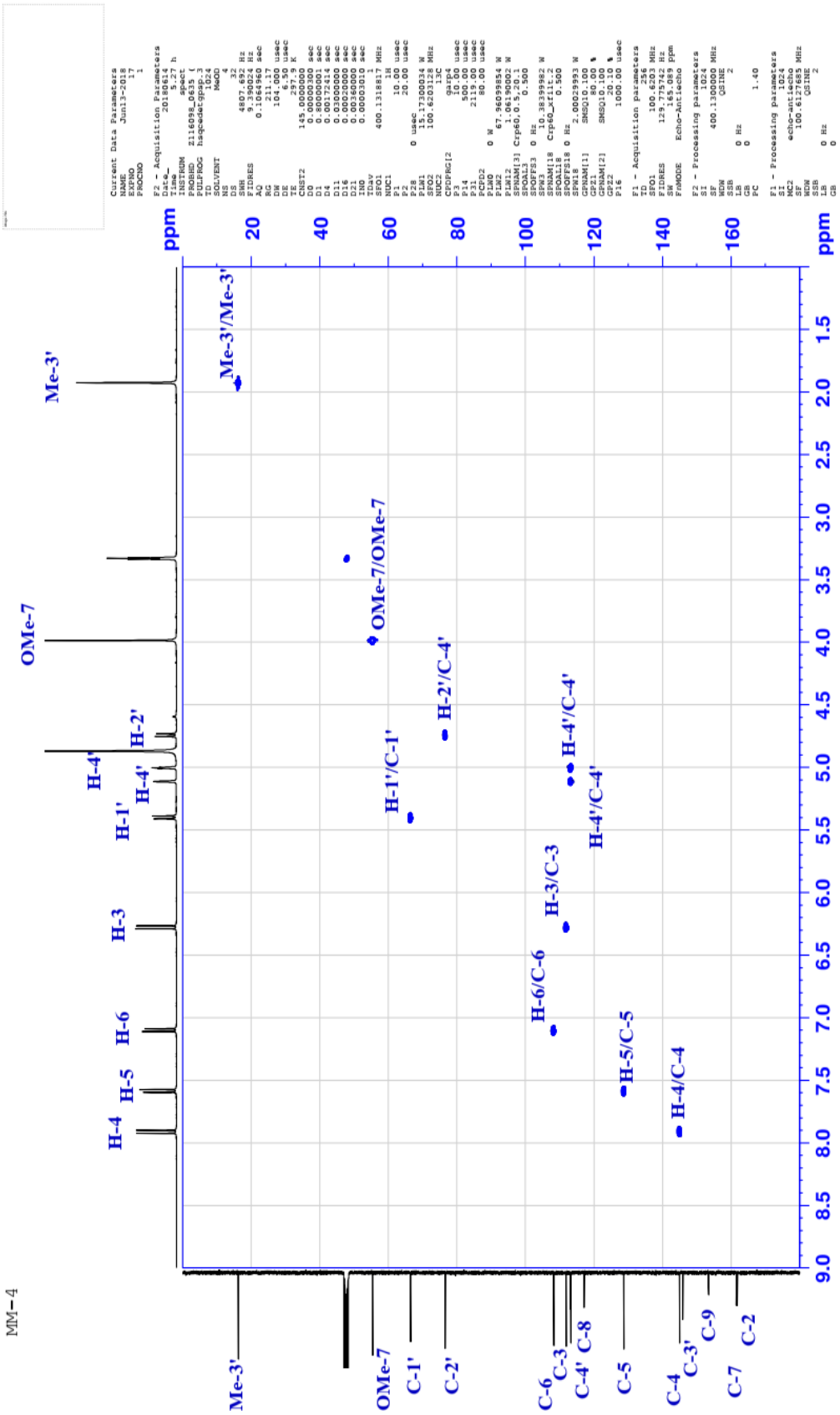

Figure S10.4. HSQC (400 MHz, $CDCl_3$) spectrum of compound 2 (MM-4)

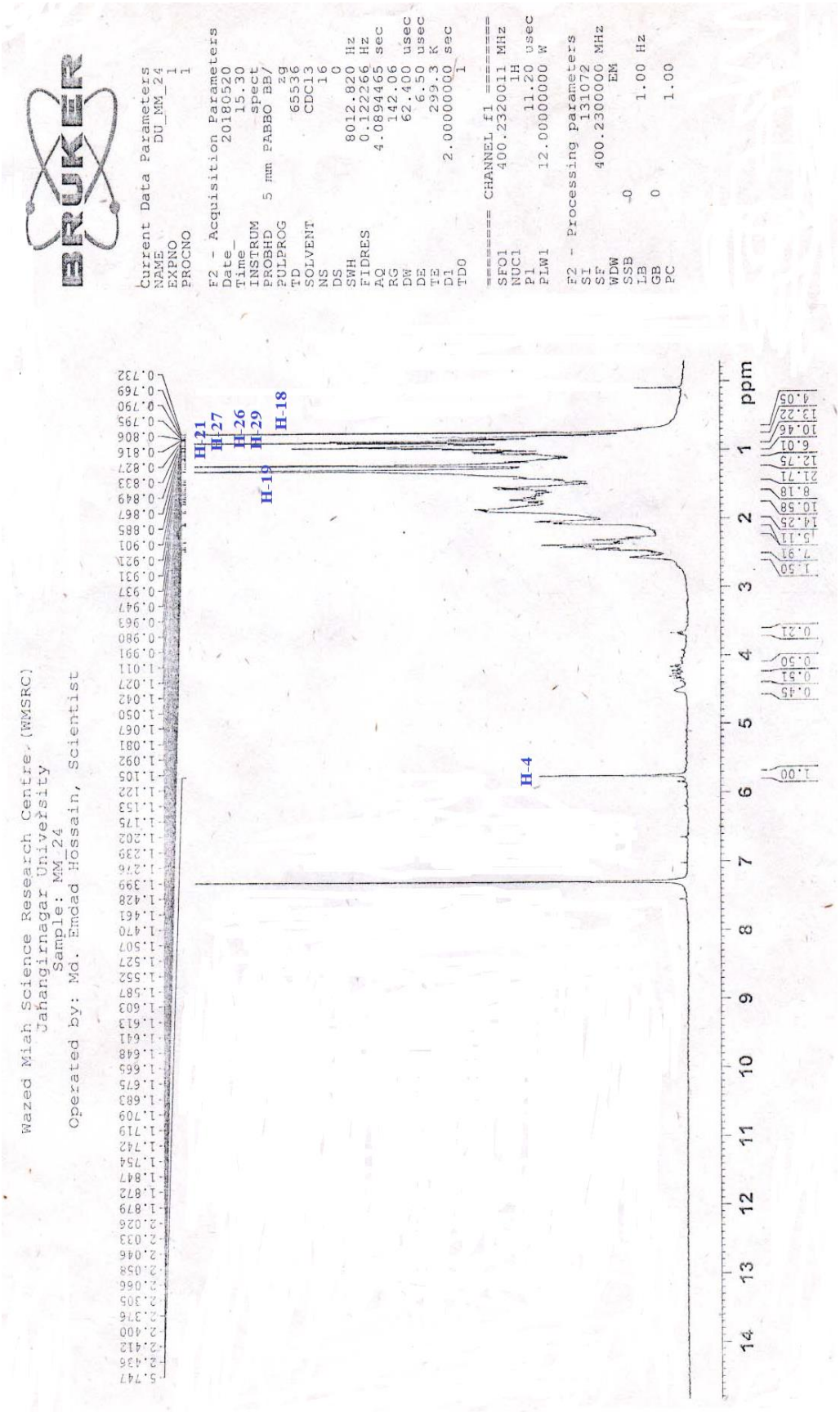

Figure S11. ^{1}H NMR (400 MHz, $CDCl_3$) spectrum of compound 3 (MM-24)

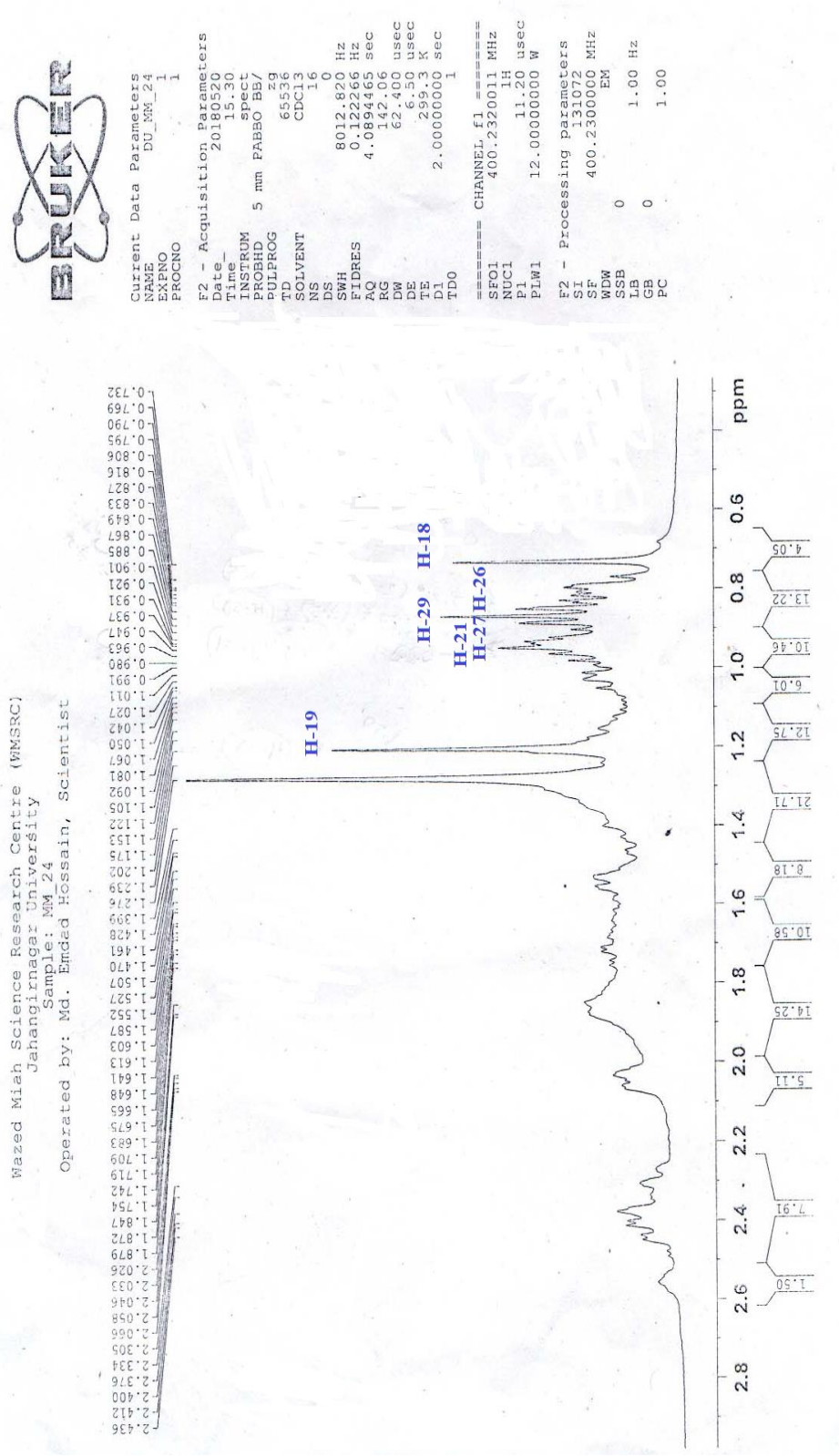

Figure S11.1. Partially expanded ^{1}H NMR (400 MHz, $CDCl_3$) spectrum of compound 3 (MM-24)